

Microstructural stability of ODS Fe–14Cr (–2W–0.3Ti) steels after simultaneous triple irradiation



M. Šćepanović^{a,*}, V. de Castro^a, T. Leguey^a, M.A. Auger^b, S. Lozano-Perez^b, R. Pareja^a

^a Departamento de Física, Universidad Carlos III de Madrid, 28911-Leganés, Spain

^b Department of Materials, University of Oxford, OX1 3PH, Oxford, UK

ARTICLE INFO

Article history:

Available online 28 August 2016

Keywords:

Oxide dispersion strengthened steels

Transmission electron microscopy

Nanoparticles

Bubbles

ABSTRACT

Simultaneous triple-ion beam irradiation experiments with Fe⁵⁺, He⁺ and H⁺ ions were performed to simulate fusion damage on two nanostructured ferritic alloys with nominal composition Fe–14Cr–0.3Y₂O₃ and Fe–14Cr–2W–0.3Ti–0.3Y₂O₃. Samples were irradiated at 600 °C to an estimated dose of ~ 30 dpa, 600 appm He, 1500 appm H, and the effects on the microstructure of these alloys investigated by analytical transmission electron microscopy. The results reveal the development of nanovoids, or small bubbles, undetected in the unirradiated samples, and a virtual compositional stability of the dispersion. Nevertheless, upon irradiation the measured size distribution indicates a slight growth of those dispersoids having the smaller sizes.

© 2016 Published by Elsevier Ltd.

This is an open access article under the CC BY-NC-ND license

(<http://creativecommons.org/licenses/by-nc-nd/4.0/>).

1. Introduction

Among the reduced activation materials developed for structural applications in the future fusion reactors and generation IV fission reactors, oxide dispersion strengthened (ODS) ferritic/martensitic and ferritic steels appear to be very promising materials. In particular, ODS and nano-structured ferritic Fe–Cr alloys may meet the criteria of microstructural stability and creep resistance under irradiation required for fusion applications [1,2]. Transmutation He and H atoms together with displacement damage will be produced at high generation rates in the structural materials, during the 14 MeV neutron irradiation in the environment of a fusion reactor. Consequently, the microstructural characteristics and the resulting mechanical properties of ODS Fe–Cr alloys can degrade depending on the irradiation conditions [3,4].

The effect of fusion damage on the microstructure can be simulated via triple beam implantation of self-ions to produce displacement damage alike to the one generated by neutron irradiation, along with He⁺ and H⁺ to simulate the concurrent presence of He and H produced by transmutation during the formation and evolution of the displacement cascades [5,6]. Moreover, the irradiation conditions during ion irradiation (dose and temperature) can be controlled easily and high doses can be achieved in short times. In

this work, simultaneous triple ion-beam irradiation has been performed to account for possible synergistic effects.

The stability of the nanoparticles present in ODS steels is critical to guarantee a good performance during service. After irradiating under different conditions, nanoparticles have been observed to grow, shrink, or remain unaltered, as recently reviewed in Refs. [7] and [8]. It appears that these changes are enhanced under ion irradiation, as compared to neutron irradiation, due to the higher dose rates used [7].

In order to gain a better understanding on the radiation damage effects in the structural material candidates for a future fusion reactor, a comprehensive analytical electron microscopy study has been performed on two nanostructured ODS Fe14Cr alloys of different compositions subjected to simultaneous triple-beam irradiation conditions that simulate those envisaged per year in a demonstration reactor (DEMO). The aim is to investigate the microstructural changes that these particular irradiation conditions can induce in these ferritic alloys, focusing on presence of bubbles and oxide nanoparticles.

2. Experimental

2.1. Materials

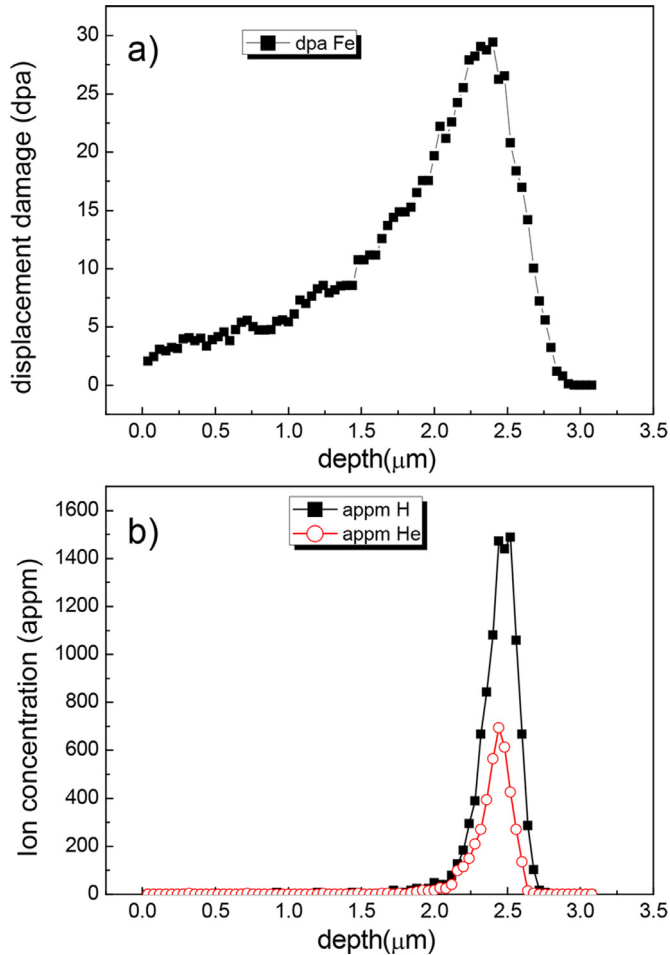
The nominal compositions of the alloys used in this work are Fe–14Cr–0.3Y₂O₃ and Fe–14Cr–2W–0.3Ti–0.3Y₂O₃ (wt%); hereafter referred to as 14YHT and 14YWTi, respectively. These alloys

* Corresponding author.

E-mail address: mšćepano@fis.uc3m.es (M. Šćepanović).

Table 1
Irradiation conditions.

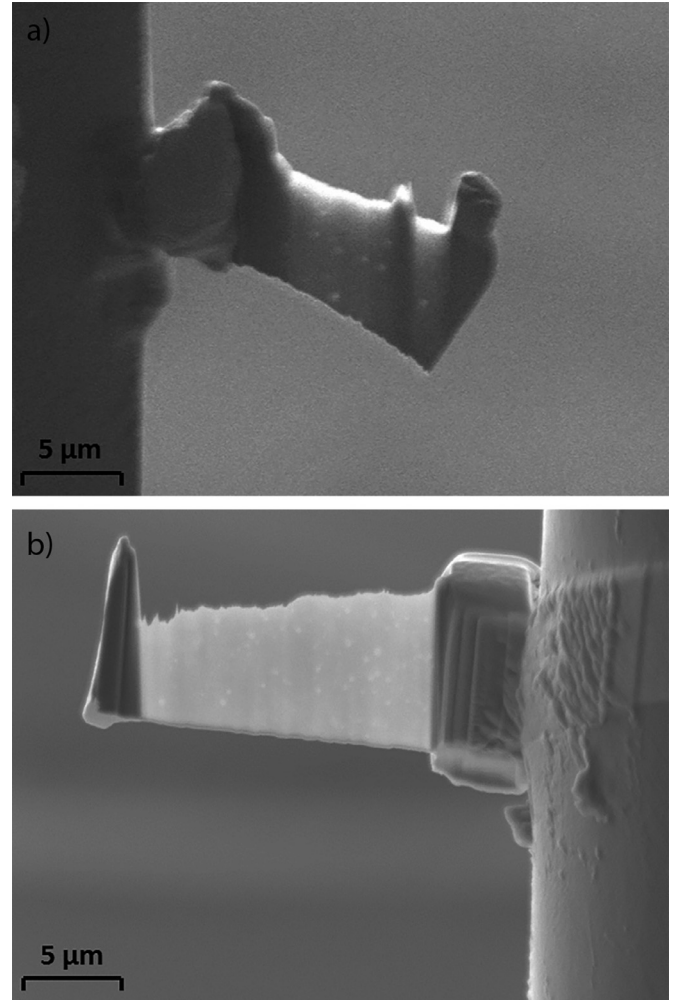
Triple irradiation JANNUS					
Ions	Energy	Temp (°C)	Dose rate (ions·cm ⁻² s ⁻¹)	Fluence (ions·cm ⁻²)	Maximum dose (dpa) / concentration (appm)
Fe ⁵⁺	14 MeV	600	8.3×10^{11}	1.49×10^{16}	~30 dpa
He ⁺	1.6 MeV		8×10^{10}	1.4×10^{15}	~600 appm
H ⁺	500 keV		1.97×10^{11}	3.55×10^{15}	~1500 appm

**Fig. 1.** SRIM damage profiles for a) Fe⁵⁺ ions and b) He⁺ and H⁺ ions.

were produced by powder metallurgy. High purity elemental powders with addition of nanosized Y₂O₃ powder were mechanically alloyed under H₂ atmosphere and consolidated by hot isostatic pressing (HIP) at 1100 °C and 200 MPa. After consolidation the alloy billets were forged at ~1150 °C and subsequently heat treated at 850 °C for 2 h. The fabrication details of these alloys are reported in Ref. [9]. The irradiation experiments were performed on 7 × 7 × 0.2 mm³ samples having their surfaces mirror polished with 50 nm alumina slurry.

2.2. Irradiation parameters

The simultaneous triple-ion irradiation with Fe⁵⁺, He⁺ and H⁺ ions was done at 600 °C to 30 dpa to simulate fusion relevant conditions. All specimens were mounted in a holder that contained a 1.1 mm diameter channel so that a thermocouple could be inserted very close to the samples for accurate temperature measurement. During irradiation, the temperature was kept at 600 ± 1 °C. The experiments were carried out at the JANNUS-Saclay Facility (France).

**Fig. 2.** Images of the a) 14YHT and b) 14YWTi alloys after focused ion beam sample preparation.

The conditions of the irradiation are summarized in Table 1. These have been specifically chosen to achieve the maximum damage at the same depth for all ions. In this case the Bragg peak is found at ~2.4 μm and limited by the minimum feasible implantation energy of the H⁺ ions (500 keV). Fig. 1 shows the damage profiles calculated by using the code SRIM2011 that simulates the damage of ions into a solid target [10]. The “full cascade” option was used to simulate all collisional damage in a Fe–14Cr target. Displacement energies of 40 eV for Fe and Cr were used, following the ASTM standard E 521–96.

2.3. TEM sample preparation and methods

Unirradiated samples for transmission electron microscopy (TEM) studies were electropolished in a TENUPO 5 twin jet polisher using a solution of 5 vol% perchloric acid in methanol as

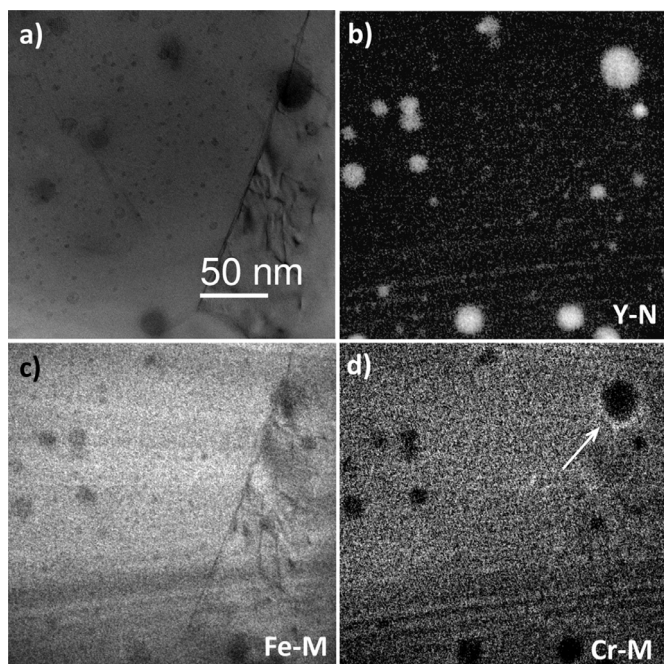


Fig. 3. a) to d) EFTEM elemental maps of the unirradiated 14YHT alloy showing the morphology and chemical composition of Y-rich nanoparticles: a) elastic image, b) Y N map, c) Fe M map, d) Cr M map, where a Cr-shell is marked with an arrow.

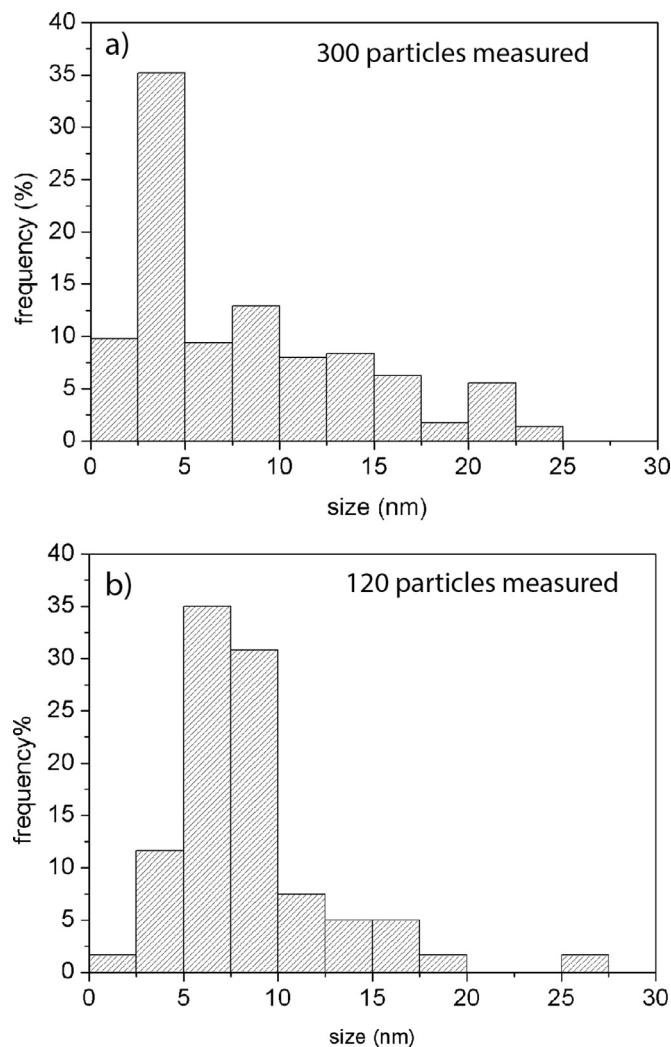


Fig. 4. Size distribution of nanoparticles in the 14YHT alloy. a) before irradiation and b) after irradiation.

electrolyte. During electropolishing, the temperature was kept below -30°C . The irradiated samples were prepared in a Zeiss AU-RIGA 40 focus ion beam (FIB) instrument fitted with a scanning electron microscope (SEM). TEM samples were prepared by the in-situ lift-out method. The different steps of the lift-out process are described as follows: a Pt layer (length = $25\text{ }\mu\text{m}$, width = $2\text{ }\mu\text{m}$, thickness < $1\text{ }\mu\text{m}$) was deposited on top of the surface in order to protect the sample during the successive milling process. A Ga^{2+} ion beam operating at 30 kV and a combination of currents ranging from 16 nA to 600 pA were used to mill material trenches on three sides of the Pt layer and underneath; as a result, a cantilever shape (length = $25\text{ }\mu\text{m}$, width = $2\text{ }\mu\text{m}$, depth = $15\text{ }\mu\text{m}$) was obtained. The micromanipulator was then used to complete the lift-out process by detaching the micromachined cantilever from the original bulk sample and attaching it to a commercial Omniprobe Cu post lift-out TEM grid. Both sides of the sample surface were milled with the Ga^{2+} ion beam at 30 kV and different currents, decreasing from 1 nA to 240 pA, until reaching electron transparency. To minimize surface artifacts induced by the FIB sample preparation, a low-energy cleaning process (2 kV and 200 pA in the Ga^{2+} ion beam) was held on both sides of the sample, obtaining the final states displayed in Fig. 2, which allowed carrying out the TEM analyses.

Imaging was done around the $2.4\text{ }\mu\text{m}$ zone, where the Bragg peak is located. Chemical information was obtained by STEM-EDS and EFTEM using a JEOL 2200MCO microscope and a JEOL ARM-200F, both operating at 200 kV beam energy. EFTEM images were processed using multivariate statistical analysis in order to separate true information from noise [11].

3. Results and discussion

3.1. Unirradiated alloys

The microstructural characteristics of the two alloys analyzed here are reported in Ref. [9]. The 14YHT alloy has a homogeneous grain structure with grains smaller than $3\text{ }\mu\text{m}$. The presence

of nanovoids could not be detected by TEM observations. Small nanoparticles and larger Cr-rich phases are present in the alloy. The nanoparticles are found dispersed homogeneously throughout the matrix, see Fig. 3a. They have Y-rich composition and further analysis reveal that they can be surrounded by Cr shells, as depicted in Fig. 3b and d. This core-shell structure was previously observed in similar ODS-Fe-(12–14 wt%)Cr steels [12,13]. It should be mentioned that the horizontal bands in the EFTEM images are an artifact caused by dirt in the omega-filter slit. Fig. 4a shows the size distribution of these particles resulting in a mean size of $8 \pm 6\text{ nm}$. It has to be noted that this distribution is likely to be skewed below 2.5 nm due to the microscope's resolution. Number densities of visible particles were measured in eight different regions. They range between $(1.2 \pm 0.2) \times 10^{21}\text{ m}^{-3}$ and $(9 \pm 2) \times 10^{22}\text{ m}^{-3}$.

The 14YWTi alloy exhibits a duplex grain structure composed of areas containing large recovered grains with sizes < $15\text{ }\mu\text{m}$, and other areas having unrecovered grains with sizes between $\sim 400\text{--}800\text{ nm}$, see Fig. 5a. Several types of secondary phases are present in this alloy, as the elemental maps in Fig. 5b–f show. There are Cr, W –rich carbides < $1.5\text{ }\mu\text{m}$ (Fig. 5c and d), Cr, Ti – rich particles having sizes ranging between $50\text{ and }500\text{ nm}$ (Fig. 5c and e) and Y–Ti-rich nanoparticles < 30 nm (Fig. 5e and f). Their mean size was reported to be $7 \pm 5\text{ nm}$ [9]. However, additional measurements have slightly shifted this value to $8 \pm 5\text{ nm}$, being within

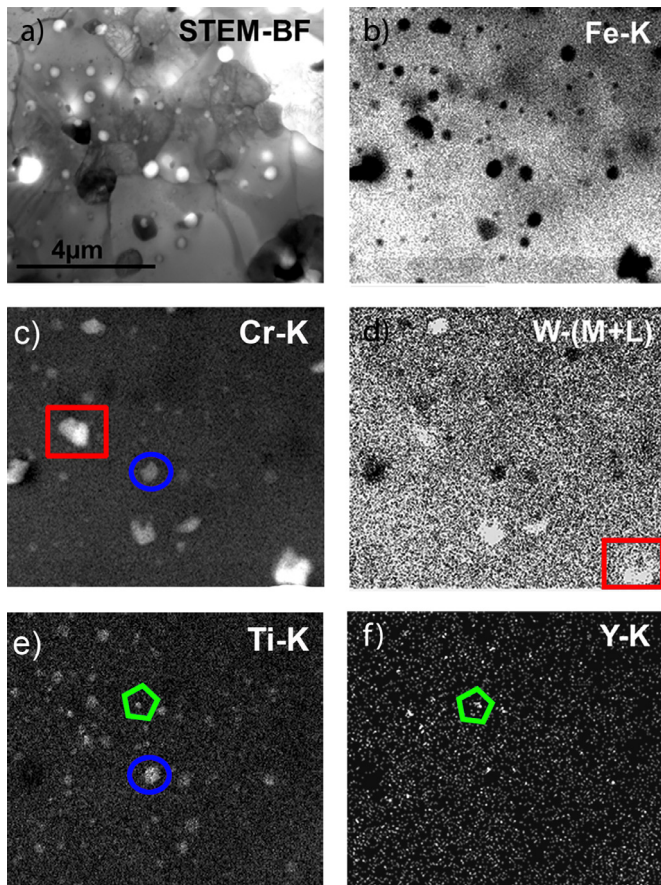


Fig. 5. a) to f) STEM image and EDS elemental maps of the unirradiated 14YWTi alloy. a) BF image, b) Fe K map, c) Cr K map, d) W (M+L) map, e) Ti K map, f) Y K map. (Cr-W rich particles are marked with a square, Cr-Ti rich with a circle and Y-Ti rich particles with a hexagon).

the error. These nanoparticles are found homogeneously dispersed throughout the matrix. Their size distribution is depicted in Fig. 6a.

Number densities of visible particles were measured in 13 different regions, ranging between $(1.2 \pm 0.2) \times 10^{21} \text{ m}^{-3}$ and $(1.3 \pm 0.3) \times 10^{22} \text{ m}^{-3}$.

3.2. Irradiated alloys

3.2.1. General microstructure

Defect evolution during irradiation may lead to dynamical recovery and recrystallization. Possible irradiation-induced changes in the general microstructure of the alloys were analyzed by performing FIB 3D slicing of the samples cross-sections. These 3D slicing results, shown in videos 1 (14YHT) and 2 (14YWTi), reveal that there are no significant changes in the grain structure of the alloys after irradiation. Representative frames of these videos are also depicted in Fig. 7. Irradiation-induced loops and defect clusters were not studied due to the fact that the irradiated samples were processed by focused ion beam, which is known to introduce defects into the sample. Slow positron annihilation measurements performed on samples of these alloys irradiated under identical conditions did not reveal evidence of implantation damage when irradiated samples were compared with unirradiated counterpart samples [14], although their penetration depth is limited to $\sim 1.2 \mu\text{m}$, while the Bragg peak is located at $\sim 2.4 \mu\text{m}$.

3.2.2. Nanoparticle evolution

It appears that the morphology and chemical composition of nanoparticles remain unchanged in both alloys after the irradiation,

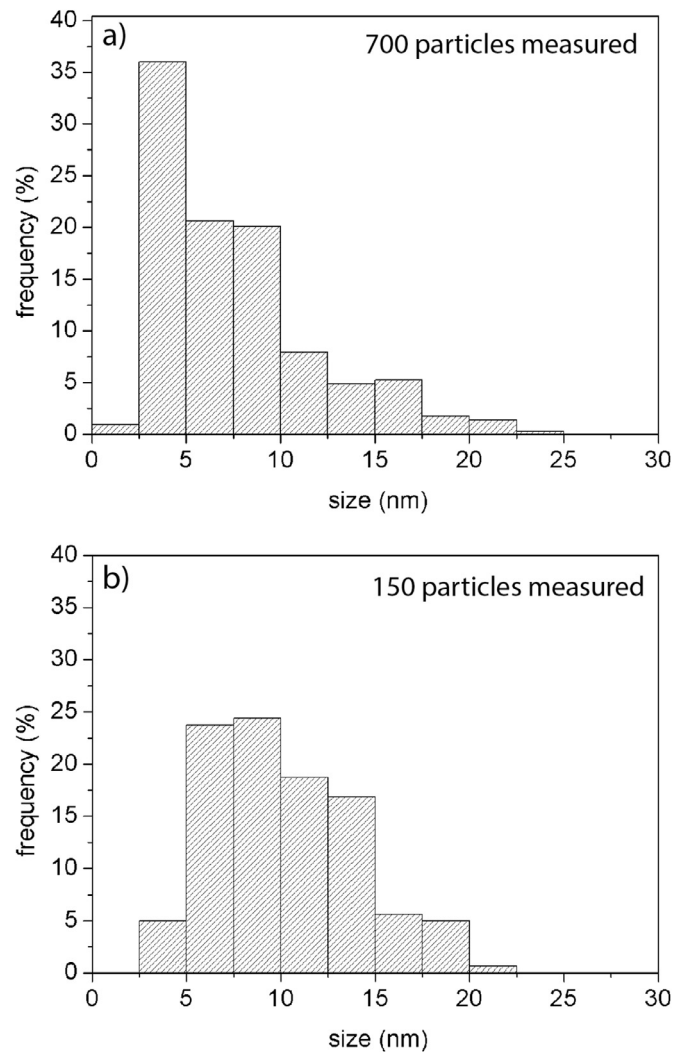


Fig. 6. Size distribution of nanoparticles in the 14YWTi alloy. a) before irradiation and b) after irradiation.

as the EFTEM and EDS maps shown in Figs. 8 and 9 reveal. Nevertheless, quantitative variations in the Ti–Y or Y–O ratios cannot be excluded. Further measurements are in progress to clarify this point.

After irradiation, number densities were measured in three different regions for the 14YHT alloy and five different regions for the 14YWTi alloy. For the 14YHT alloy, they vary between $(1.8 \pm 0.4) \times 10^{21} \text{ m}^{-3}$ and $(3.2 \pm 0.6) \times 10^{22} \text{ m}^{-3}$, and between $(3.5 \pm 0.7) \times 10^{21} \text{ m}^{-3}$ and $(6.9 \pm 1.4) \times 10^{21} \text{ m}^{-3}$ for the 14YWTi alloy. These densities lie within the density ranges found in the unirradiated alloys. In both alloys, the maximum density value is lower than the corresponding for the unirradiated while the minimum density value is similar. It has to be taken into account that less regions were measured for the irradiated alloys due to lack of irradiated material (only those volumes of the FIB sample around the Bragg peak can be studied). Consequently, it appears that the densities are similar after irradiation. However, the size distributions shown in Figs. 4b and 6b indicate some changes in the particle size distribution. Even though the mean size of nanoparticles has remained very similar, i.e. $8 \pm 4 \text{ nm}$ for 14YHT and $10 \pm 4 \text{ nm}$ for 14YWTi, it appears that there has been a slight coarsening of particles having smaller sizes than 5 nm before irradiation at least for the studied regions. Previous works on model ODS alloy have shown that after dual beam irradiations with Fe

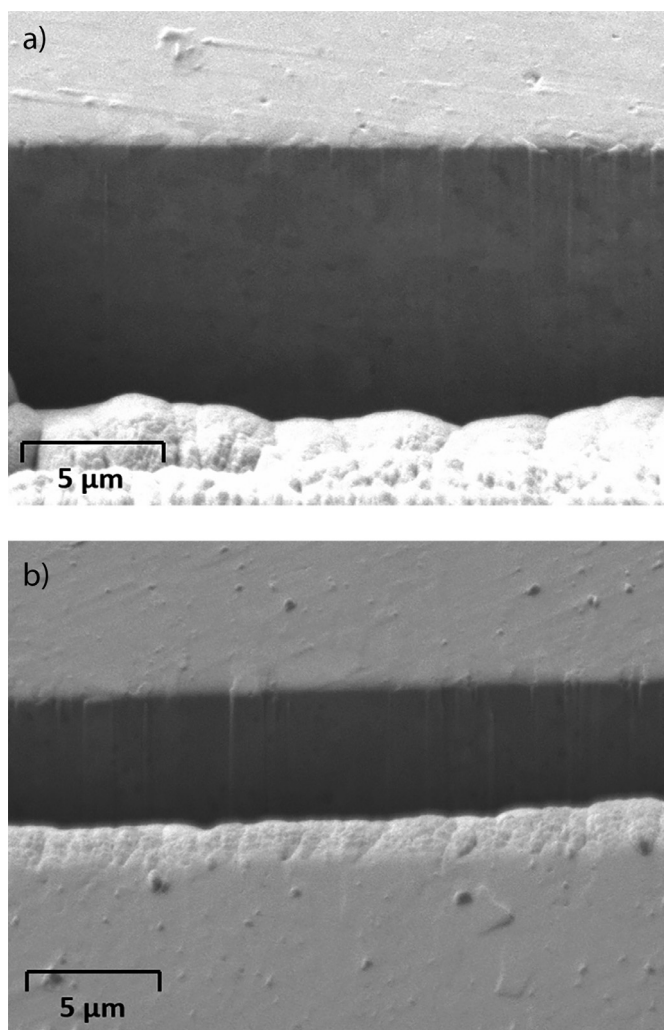


Fig. 7. SEM 3D slicing image showing the grain structure of a) irradiated 14YHT and b) irradiated 14YWTi.

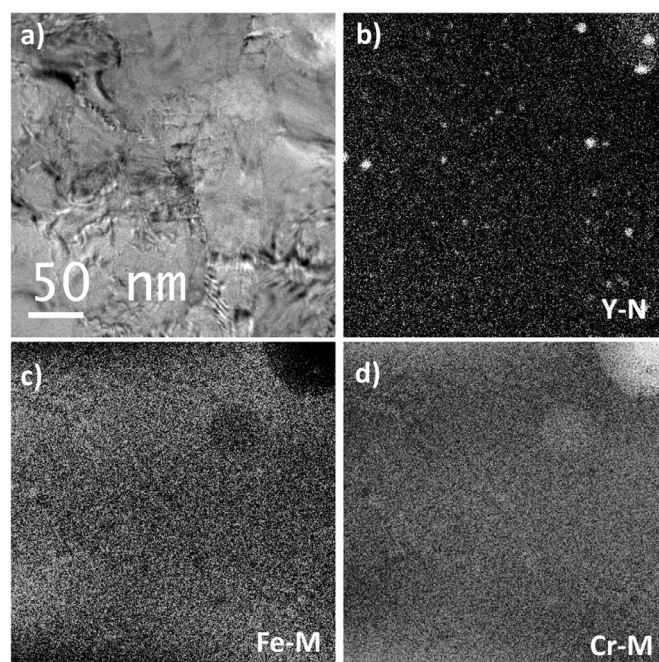


Fig. 8. a) to d) EFTEM elemental maps of the irradiated 14YHT alloy showing the morphology and chemical composition of Y-rich nanoparticles: a) elastic image, b) Y N map, c) Fe M map, d) Cr M map.

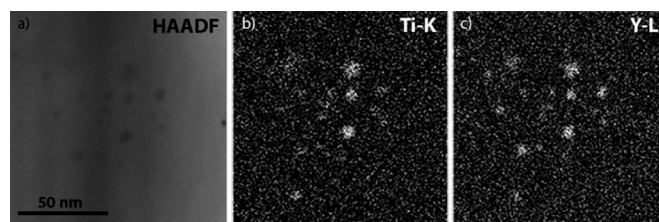


Fig. 9. a) to c) STEM image and EDS elemental maps of the irradiated 14YWTi alloy. a) HAADF image, b) Ti K map, c) Y L map.

and He (80 dpa/360 appm) done at 600 °C, particles are in average coarser than the ones prior to irradiation [15]. Also, the study of the microstructural evolution of a neutron irradiated ODS ferritic steel, to a dose of 100 dpa at temperatures of 500 and 700 °C has shown that the sizes of oxides increased when compared to the unirradiated ones [16]. Particle growth was also observed in ODS (14–18)Cr ferritic steels irradiated by 500 keV Fe ions to 150 dpa maintaining the temperature of 500 °C, which is in accordance with our results [7,17]. Moreover, the same ODS 14Cr steel irradiated with neutrons to 75 dpa also shows particle growth although the growth rate is smaller than in the ion irradiated steel [7].

3.2.3. Irradiation induced bubbles

The analyses of the 14YHT and 14YWTi samples after triple-ion beam irradiation under the present conditions reveal the presence of small irradiation-induced bubbles, most of them with sizes < 4 nm. These bubbles are located either in the matrix or at particle-matrix interfaces, see Figs. 10 and 11, where Fresnel contrast was used to reveal them as bright dots in underfocused images (Figs. 10 and 11 (a)) and as dark dots in overfocused ones (Figs. 10 and 11 (c)). Previous studies of a non-ODS Fe–12Cr alloy simultaneous triple-ion beam irradiated with Fe³⁺ (50 dpa), He⁺ (500 appm) and H⁺ (2000 appm) show that the swelling peak is found at ~510 °C, and the bubble sizes decrease in the case of irradiation at 600 °C, which is consistent with the present results [18].

4. Conclusions

This paper reports TEM analyses of two ferritic ODS steels simultaneously triple-beam irradiated at 600 °C under conditions that simulate the expected fusion damage in DEMO after one year. The nanoparticles in both samples appear to have maintained their composition and morphology after the triple-ion beam irradiation, while their sizes appear to increase slightly. The most prominent change induced by the irradiation under the present conditions was the development of small bubbles in the matrix or associated to nanoparticles.

Acknowledgments

This investigation was supported by the Ministerio de Economía y Competitividad (project ENE2012-39787-C6-05), the Comunidad de Madrid through TECHNOFUSION-II (S2013/MAE-2745), the Royal Society, the European Commission through the European Fusion Development Agreement (EFDA), and the EU FP7 through the Integrated Infrastructure Initiative-I3 (Grant Agreement 312483 - ES-TEEM2). The authors acknowledge the JANNUS-Saclay team for their scientific and technological advice, support from the EP-SRC programme grant “Materials for Fusion and Fission Power” (EP/H018921/1) and EPSRC (grant EP/K040375/1) for the ‘South of England Analytical Electron Microscope’.

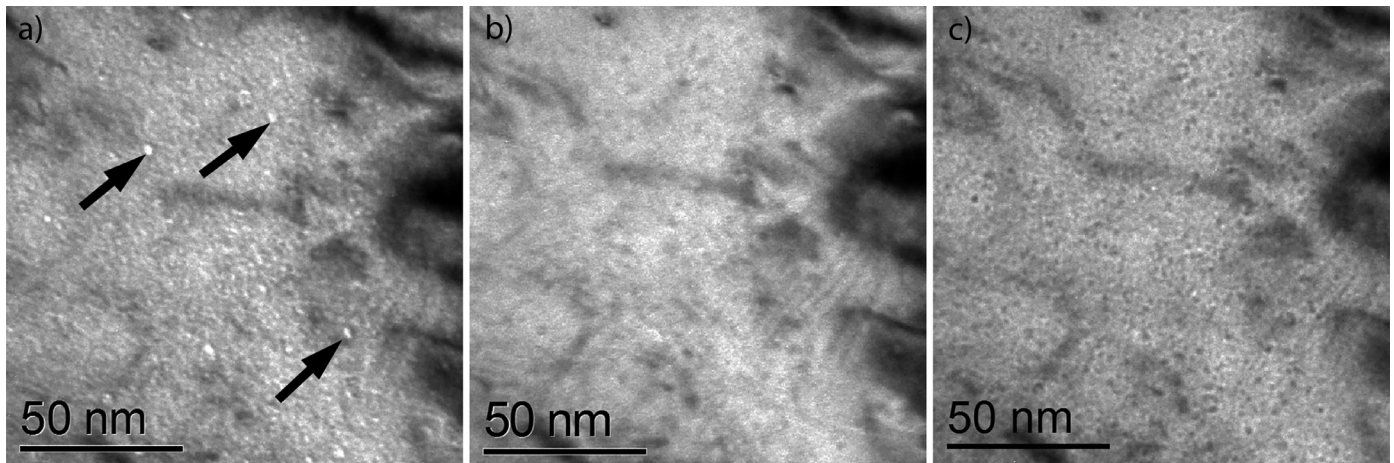


Fig. 10. Through-focal series of irradiation induced bubbles in the 14YHT alloy. a) underfocused by 1 μm , b) in focus and c) overfocused by 1 μm . Some bubbles are marked with an arrow in the underfocused image.

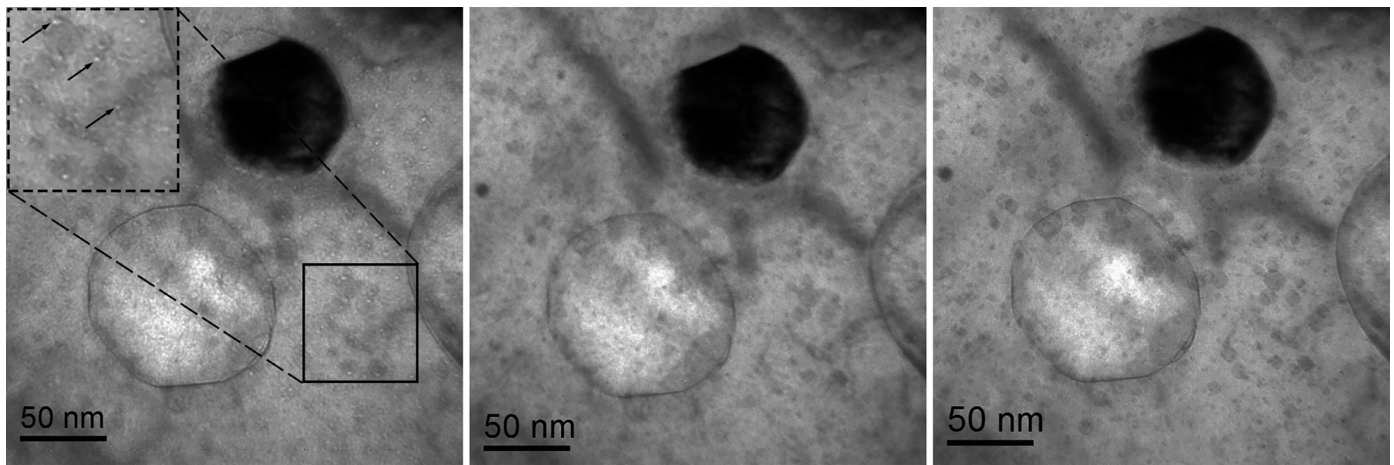


Fig. 11. Through-focal series of irradiation induced bubbles in the 14YWTi sample. a) underfocused by 1 μm , b) in focus and c) overfocused by 1 μm . Some bubbles are marked with an arrow in the underfocused image.

Supplementary materials

Supplementary material associated with this article can be found, in the online version, at [doi:10.1016/j.nme.2016.08.001](https://doi.org/10.1016/j.nme.2016.08.001).

References

- [1] R.E. Stoller, *Compr. Nucl. Mater.* 1 (2012) 293–332.
- [2] R.L. Klueh, D.R. Harries, *High-Chromium Ferritic and Martensitic Steels for Nuclear Applications*, ASTM, West Conshohocken, US, 2001.
- [3] N. Baluc, J.L. Boutard, S.L. Dudarev, M. Rieth, J. Brito Correia, B. Fournier, J. Henry, F. Legendre, T. Leguey, M. Lewandowska, R. Lindau, E. Marquis, A. Munoz, B. Radiguet, Z. Oksiuta, *J. Nucl. Mater.* 417 (2011) 149–153.
- [4] A. Kimura, R. Kasada, A. Kohyama, H. Tanigawa, T. Hirose, K. Shiba, S. Jitsukawa, S. Ohtsuka, S. Ukai, M.A. Sokolov, R.L. Klueh, T. Yamamoto, G.R. Odette, *J. Nucl. Mater.* (2007) 60–67 367–370.
- [5] G.S. Was, R.S. Averback, *Compr. Nucl. Mater.* 1 (2012) 195–221.
- [6] J. Marian, T. Hoang, M. Fluss, L.L. Hsiung, *J. Nucl. Mater.* 462 (2015) 409–421.
- [7] J. Ribis, E. Bordas, P. Trocellier, Y. Serruys, Y. de Carlan, A. Legris, *J. Mater. Res.* 30 (2015) 2210–2221.
- [8] V. de Castro, S. Lozano-Perez, M. Briceno, P. Trocellier, S. Roberts, R. Pareja, *J. Mater. Sci.* 50 (2015) 2306–2317.
- [9] M.A. Auger, V. de Castro, T. Leguey, M.A. Monge, A. Muñoz, R. Pareja, *J. Nucl. Mater.* 442 (2013) S142–S147.
- [10] J.F. Ziegler, U. Littmark, J.P. Biersack, *The Stopping and Range of Ions in Solids*, Pergamon Press, Pergamon, New York, 1985.
- [11] S. Lozano-Perez, *J. Phys.* 126 (2008) 012040.
- [12] V. de Castro, E.A. Marquis, S. Lozano-Perez, R. Pareja, M.L. Jenkins, *Acta Mater.* 59 (2011) 3927–3936.
- [13] V. de Castro, T. Leguey, M.A. Auger, S. Lozano-Perez, M.L. Jenkins, *J. Nucl. Mater.* 417 (2011) 217–220.
- [14] P. Parente, T. Leguey, V. de Castro, T. Gigl, M. Reiner, C. Hugenschmidt, *J. Nucl. Mater.* 464 (2015) 140–146.
- [15] C. Robertson, B.K. Panigrahi, S. Balaji, S. Kataria, Y. Serruys, M.-H. Mathon, C.S. Sundar, *J. Nucl. Mater.* 426 (2012) 240–246.
- [16] S. Yamashita, N. Akasaka, S. Ukai, S. Ohnuki, *J. Nucl. Mater.* (2007) 202–207 367–370.
- [17] M.L. Lescoat, J. Ribis, Y. Chen, E.A. Marquis, E. Bordas, P. Trocellier, Y. Serruys, A. Gentils, O. Kaitasov, Y. de Carlan, A. Legris, *Acta Mater.* 78 (2014) 328–340.
- [18] T. Tanaka, K. Oka, S. Ohnuki, S. Yamashita, T. Suda, S. Watanabe, E. Wakai, *J. Nucl. Mater.* (2004) 294–298 329–333.